Spindle Oscillation Emerges at the Critical State of the Electrically Coupled Network in Thalamic Reticular Nucleus

A PREPRINT

Shangyang Li[1] *
syli@pku.edu.cn

Chaoming Wang[1] *
wangchaoming@pku.edu.cn

Si Wu[1]†
siwu@pku.edu.cn

[1]Peking-Tsinghua Center for Life Sciences, Academy for Advanced Interdisciplinary Studies,
School of Psychological and Cognitive Sciences,
Beijing Key Laboratory of Behavior and Mental Health,
IDG/McGovern Institute for Brain Research,
Center of Quantitative Biology, Peking University.

December 31, 2023

ABSTRACT

Spindle oscillation is a waxing-and-waning neural oscillation observed in the brain, initiated at the thalamic reticular nucleus (TRN) and typically occurring at $7-15$ Hz. Recent experiments revealed that in the adult brain, electrical synapses, rather than chemical synapses, are dominating between TRN neurons, indicating that the traditional view of spindle generation via chemical synapses in the TRN needs to be revised. Here, based on the known experimental data, we develop a computational model of the TRN network, in which heterogeneous neurons are connected by electrical synapses. The model consists of two driving forces competing to shape the network dynamics: electrical synapses tend to synchronize neurons, while heterogeneity tends to desynchronize neurons. We demonstrate that the interplay between two forces leads to a network state where multiple synchronized clusters with slightly different oscillation frequencies coexist. In this state, the superposition of neuronal activities gives rise to spindle oscillation, as observed in local field potentials in experiments. Notably, we discover that when TRN neurons generate spindle oscillation, the network operates at the critical state, known for facilitating efficient information processing in complex systems. Our study sheds light on the underlying mechanism of spindle oscillation and its functional significance in neural information processing.

Keywords Spindle Oscillation · Electrical Synapse · Neuronal Heterogeneity · Critical State · Thalamic Reticular Nucleus

1 Introduction

Spindle oscillation refers to a waxing-and-waning oscillatory event occurring at a frequency of $7-15$ Hz [1]. This phenomenon has been widely observed in various mammals, including the cat [2, 3], mice [4, 5], rat [6, 7], ferret [8, 9], dog [10, 11], sheep [12], macaque [13, 14], and human [15, 16]. Extensive experimental studies have established a strong correlation between spindle oscillation and learning and memory processes in the brain [17]. For example, research has shown that the density and amplitude of spindle oscillation increase during post-learning sleep, both for declarative memory tasks [18, 19, 20] and procedural memory tasks [21, 22]. Manipulation studies conducted on humans and rodents have provided causal evidence supporting the role of spindle oscillation in memory consolidation [23, 24]. Despite the recognized importance of spindle oscillation in brain functions, the neural mechanism underlying spindle generation remains a subject of debate.

*These authors contributed equally to this work.
†Corresponding author.

The conventional understanding of spindle generation has suggested that spindles are generated in the thalamus [1, 25, 16]. For example, early investigations on anesthetized cats revealed that the decorticated thalamus alone could produce waxing-and-waning spindle rhythms [26, 27]. In vitro studies using thalamic slices further demonstrated that the synaptic connectivity between thalamocortical (TC) relay neurons and thalamic reticular nucleus (TRN) neurons played a crucial role in spindle rhythm generation [28, 29, 30, 8, 31, 9]. According to this framework, low-threshold bursts from TRN cells transiently inhibit TC neurons, and upon release from inhibition, TC cells generate Ca^{2+}-dependent post-inhibitory rebound bursts, which drive subsequent spike bursts in TRN neurons [25, 32, 33, 34, 35]. However, recent experimental findings have challenged this "ping-pong" model of spindle generation. These inconsistencies include: 1) optogenetic stimulation of TRN neurons triggering cortical spindles that are not observed in the corresponding TC site [36]; 2) the generation of sleep spindles in the mouse thalamus in the absence of T-type Ca^{2+} channels and burst firing of TC neurons, both in vivo and in vitro [37]; and 3) administration of a Ca^{2+} channel blocker in the corticothalamic network reducing spindles at higher frequencies (approximately 14 Hz) while enhancing the power of slow spindles (approximately 10 Hz) [38]. These inconsistencies strongly suggest that the involvement of TC cells is not the necessary condition for spindle generation [32].

Earlier studies have suggested that the TRN alone can generate oscillations at the spindle frequency without inputs from the cortex and thalamus [3, 39, 40]. TRN neurons are intrinsic GABAergic cells that encompass the entire thalamus [41, 42]. They receive glutamate excitatory inputs from TC and corticothalamic (CT) neurons [41, 43], as well as extensive inhibitory projections from subcortical areas, including the basal forebrain [44, 45, 46, 47], the substantia nigra pars reticulata [48], the globus pallidus [49, 50, 51], and the hypothalamus [52]. Earlier experiments involving local glutamate application revealed that TRN neurons in rodents younger than 2 weeks of age are interconnected through inhibitory chemical synapses [53, 54, 55, 56, 57]. Subsequent computational modeling demonstrated that an isolated TRN network, with neurons connected by inhibitory chemical synapses, can generate various types of network oscillations at frequencies of 7-10 Hz [58, 33, 59, 60]. However, these models rely on low-threshold Ca^{2+}-dependent bursts, which either require a sufficiently negative reversal potential of inhibitory synapses [58, 33, 59] or a hyperpolarized resting membrane potential [60]. These assumptions are not consistent with the biological properties of TRN neurons, which include: 1) TRN cells have a depolarized chloride reversal potential ($\mathrm{E_{GABA}} = -62$ mV) compared to TC neurons, resulting in postsynaptic depolarizations rather than strong inhibition upon receiving GABAergic inputs [61, 62, 63]. 2) Spindles can be generated from isolated TRN slices with a more depolarized resting potential (-63.8 $\pm$ 1.2 mV) [30, 28].

Moreover, recent experiments have shown that electrical synapses dominate the connectivity between TRN neurons after two weeks of age. Paired recordings from TRN neurons in rats and mice across different ages have revealed the presence of electrical synapses but rare chemical transmission between TRN neurons [64, 65, 66, 67, 68]. Optogenetic stimulation of layer 6 CT neurons or neighboring TRN neurons failed to evoke inhibitory postsynaptic currents (IPSCs) in TRN neurons in mice older than two weeks [69, 70, 71]. Genetic deletion of vesicular GABA transporters from TRN neurons only reduced GABAergic transmission in TC neurons but not TRN neurons [71]. These findings indicate that the electrically coupled TRN network, without direct inputs from TC neurons, is sufficient for the generation of spindle oscillations. Notably, sleep spindles begin to emerge around 2-3 months of age in humans and during the third to fourth postnatal weeks in rodents [72], which aligns with the dominance of electrical couplings in the TRN at later developmental stages. Thus, the traditional mechanism based on chemical synapses for spindle generation in the TRN needs to be revisited.

Motivated by the newly accumulated experimental evidence, the present study investigates the generation of spindle oscillation within the electrically coupled TRN neurons. We have developed a computational model that incorporates the latest findings regarding TRN neurons, specifically the prevalence of electrical synapses between neurons and the presence of neuronal heterogeneity. These factors have opposing effects on network dynamics, as electrical coupling tends to synchronize neurons while neuronal heterogeneity tends to desynchronize them. Our study demonstrates that the interplay between electrical coupling and neuronal heterogeneity leads to the self-organization of the TRN network into the critical state. In this state, neurons form multiple synchronized clusters, each oscillating at slightly different frequencies. The superposition of these neuronal activities, mimicking the local field potential (LFP) recorded in experiments, exhibits characteristic spindle oscillations. Overall, our modeling study uncovers a natural emergence of spindle oscillations within the TRN network when it operates in the critical state — a condition known to facilitate efficient information processing in complex systems [73]. These findings shed light on the underlying mechanisms of spindle generation and provide further insights into the functional role of the TRN in regulating thalamocortical activity.

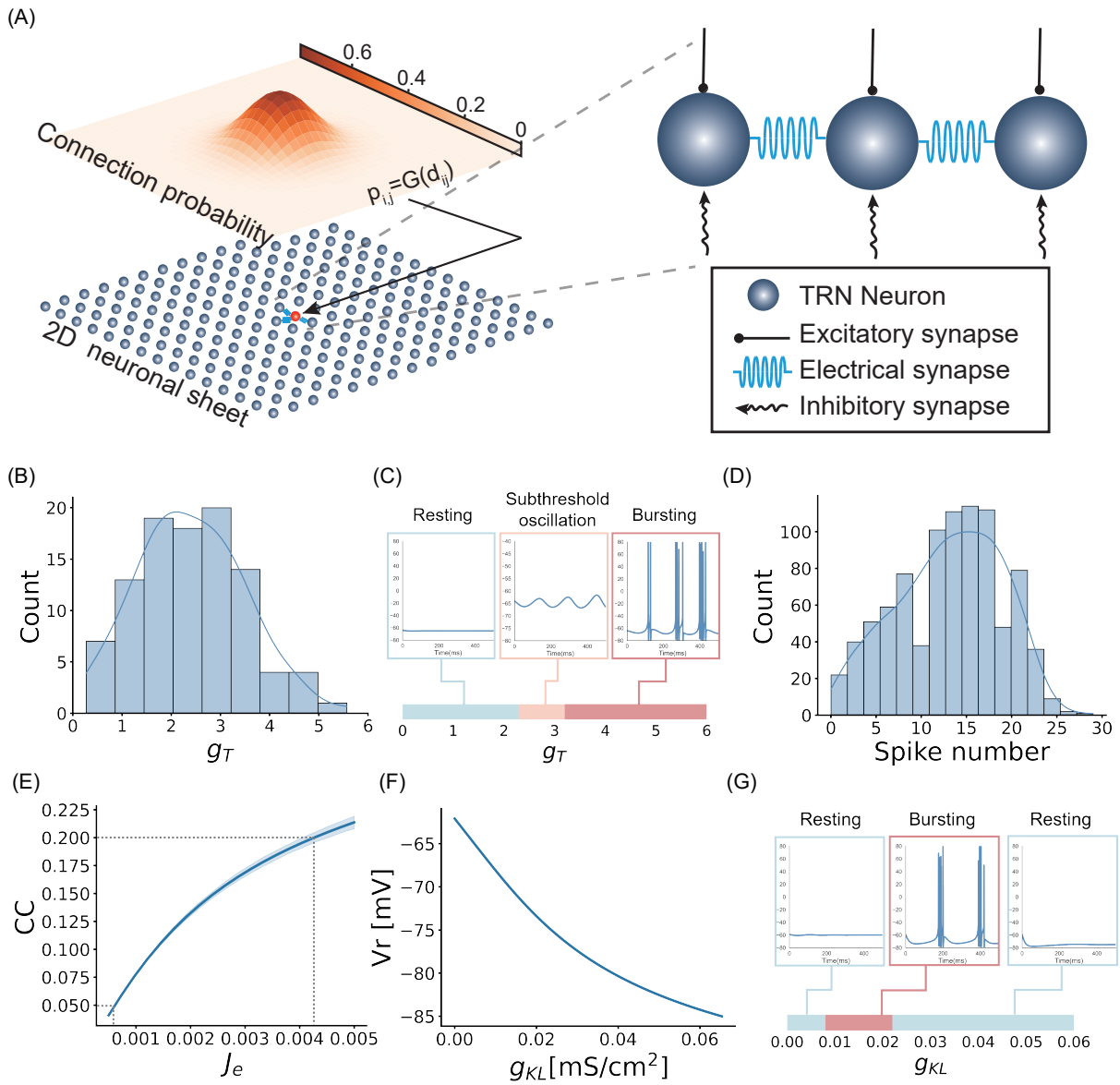

Figure 1: The TRN network model. (A) The network structure. TRN neurons are uniformly distributed on a two-dimensional sheet and connected with electrical synapses. The connection probability between neurons follows a distance-dependent Gaussian distribution. Each neuron receives an excitatory thalamic and cortical input and an inhibitory subcortical input. (B) The distribution of the conductance g_T of T-type Ca^{2+} channels of all TRN neurons. (C) The spontaneous activity of a TRN neuron changes from the resting state, subthreshold oscillation, to bursting firing when increasing the conductance g_T. (D) The distribution of the number of spikes per burst in TRN neurons. Each burst was triggered by injecting a negative current followed by abrupt current removal [74]. (E) The relationship between the coupling coefficient and the conductance of electrical synapse J_e. For CC in the range of $(0.05 - 0.2)$, J_e is in the range of $(0.0005, 0.005)$. (F) The relationship between the resting membrane potential and the potassium leaky conductance g_{KL}. (G) The spontaneous activity of a TRN neuron changes from the resting state, bursting firing, to the resting state when increasing the neuromodulation level g_{KL}.

2 Results

2.1 An electrically coupled heterogeneous TRN network

We built a TRN network model according to the latest physiological data collected from ferrets, cats, mice, and rats. Specifically, we considered that the TRN network is a two-dimensional grid (Figure 1A), on which N neurons are uniformly distributed and connected with each other by electrical synapses [64, 65, 67, 68, 71] according to a Gaussian probability connection profile (this reflects the fact that neighboring TRN neurons tend to be connected by electrical synapses [67], see details in Methods and Materials). Each neuron in the network receives two kinds of external synaptic inputs: excitatory synaptic projections from the thalamus and cortex [41], and inhibitory inputs from subcortical brain areas [44, 45, 46, 47, 48, 49, 50, 51, 52]. The dynamics of a single TRN neuron is given by [75],

$$\tau \frac{\mathrm{d}V}{\mathrm{d}t} = I_{\mathrm{L}} + I_{\mathrm{Na}} + I_{\mathrm{K}} + I_{\mathrm{T}} + I_{\mathrm{KL}} + I_{\mathrm{gap}} + I_{\mathrm{inh}} + I_{\mathrm{exc}}, \tag{1}$$

where V is the membrane potential and τ the membrane time constant. I_L, I_{Na}, I_{K}, I_{T} and I_{KL} denote, respectively, the leaky channel current, the sodium channel current, the potassium channel current, the low-threshold calcium channel current, and the potassium leaky current. I_{gap} denotes the recurrent gap junctional current from other TRN neurons. I_{inh} and I_{exc} denote the subcortical inhibitory current [51, 52] and the thalamic and cortical excitatory current [41, 43], respectively. For the detailed form of each current, see Methods and Materials.

In the experiments, spindle oscillation was observed in the local field potential (LFP). In our model, we considered that the simulated LFP represents the averaged membrane potential of all TRN neurons, which is calculated to be,

$$\mathrm{LFP} = \frac{1}{N} \sum_{i=1}^{N} \mathrm{V}_i, \tag{2}$$

where V_i is the membrane potential of the ith neuron, and the summation runs over all TRN neurons.

In our model, the generation of spindle oscillation is influenced by three crucial factors: neuron heterogeneity, electrical couplings between neurons, and neuromodulation levels. In the below, we will discuss the settings of these factors in the model and explore their effects on the neural dynamics.

Heterogeneity of TRN neurons. TRN neurons are distinguished by their abundant T-type Ca^{2+} channels [76]. In our model, we computed the T-type Ca^{2+} channel current using the equation $I_T = g_T f(V)$ (refer to Eq.5 for the specific form of $f(V)$), where g_T represents the channel conductance. It is important to note that TRN neurons exhibit significant heterogeneity. Different TRN neurons display distinctive firing patterns, which have been linked to variations in sleep rhythms across sensory cortices [77, 78]. One of the primary sources of this heterogeneity is the varied distribution of T-type Ca^{2+} channels among TRN neurons [79, 80, 78, 77, 81, 74]. Therefore, in our model, we assigned different values of g_T to individual neurons to reflect this heterogeneity (see Figure1B).

We explored how g_T affects the dynamics of a single neuron. By varying g_T, we observed that (Figure 1C): 1) for $g_T < 2.32\ \mathrm{mS/cm^2}$, the neuron is in the resting state; 2) for $2.32\ \mathrm{mS/cm^2} < g_T < 3.19\ \mathrm{mS/cm^2}$, subthreshold oscillation occurs as seen in the voltage clamp experiment [65], and the amplitude of subthreshold oscillation increases with g_T; 3) for $g_T > 3.19\ \mathrm{mS/cm^2}$, the neuron generates bursting spikes.

To match with the experimental data, we considered that the values of g_T for all neurons are randomly sampled from a truncated normal distribution as illustrated in Figure 1B. In the biological experiment, the number of spikes per offset burst of TRN neurons was measured and was found to approximately satisfy a normal distribution (Fig. 3D in [74]). Following the same protocol as in [74], we injected a negative current to a TRN neuron followed by a sudden current removal to induce bursting firing of the neuron. We set the distribution of g_T appropriately, such that the numbers of spikes in bursts generated by all TRN neurons exhibit a similar distribution as observed in the experiment (Figure1D).

Electrical couplings between TRN neurons. Another remarkable feature of TRN neurons is their electrical couplings [64, 65, 71]. In the model, we set the electrical synapse current between neurons (i, j) to be $I_{gap} = J_e(V_j - V_i)$ (see Methods and Materials 4.3 for details), with J_e the coupling conductance. The strength of electrical couplings can be quantified by the coupling coefficient (CC) between TRN neurons (Methods and Materials 4.3). To correlate the electrical synapse conductance J_e with the CC, we calculated how the average CC varies with J_e (see Figure 1E). To be consistent with the experimental finding that the average CC in TRN varies in the range of $(0.05 - 0.2)$ [65, 82], we set the conductance J_e of electrical synapse in the range of $(0.0005, 0.005)$ in all later computational experiments.

Modulation by neuromodulators. It is known that subcortical neuromodulators, such as acetylcholine and norepinephrine, influence oscillatory activities in the thalamus [83, 84]. To model this neuromodulation effect, we included

a potassium leaky current $I_{KL} = g_{KL}(E_{KL} - V)$ in the neuronal dynamics (see Eq. 5 for more details), where g_{KL} is the conductance controlled by neuromodulators. At the single neuron level, g_{KL} shows a great impact on the membrane resting potential, i.e., the value of resting potential decreases with g_{KL} (Figure 1G). Neuromodulation also affects neuronal firing patterns. As illustrated in Figure 1F, a TRN neuron tends to oscillate at an intermediate g_{KL} value and rest when g_{KL} is small or large.

2.2 Spindle oscillation emerges in the TRN network

Experimental studies have revealed various oscillation behaviors in the TRN network during different sleep and awake conditions [85]. To validate our network model, we first identify the parameter ranges in which TRN spindles occur. Specifically, we manipulate the parameter g_{KL}, which reflects the levels of neuromodulation in different sleep and awake conditions, while keeping all other parameters constant at appropriate values (see Methods and Materials). Furthermore, we incorporate an inhibitory current I_{inh} from subcortical regions when modeling the sleep condition, while excluding any excitatory current I_{exc} from the thalamic and cortical regions. Conversely, in the awake condition, we include both I_{inh} and I_{exc}.

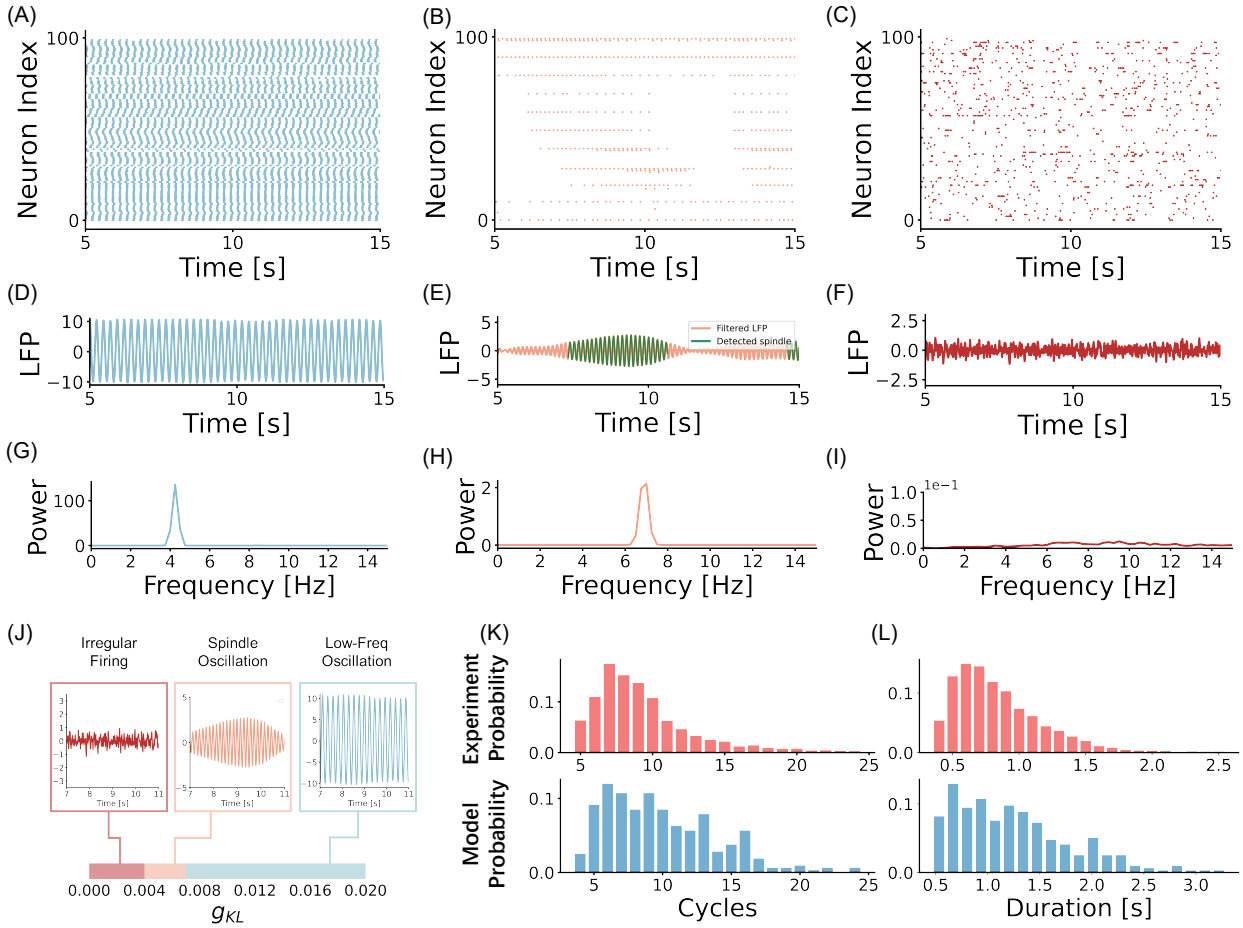

Figure 2: Oscillation behaviors of the TRN Network. (A-C) Raster plots of neurons' firings in deep sleep, light sleep, and alertness conditions, respectively. (D-F) LFP in deep sleep, light sleep, and alertness conditions, respectively. (G-I) The spectrum of LFP in deep sleep, light sleep, and alertness conditions, respectively. (J) The phase diagram of the network state with respect to the neuromodulation level g_{KL}. (K) The statistical properties of the spindle oscillation cycle in experiments [6] and our model. Upper panel: the experimental data. Lower panel: the model simulation data. (L) The statistical properties of the spindle oscillation duration in experiments [6] and our model. Upper panel: the experimental data. Lower panel: the model simulation data.

Deep sleep condition. In deep sleep, i.e., N3 NREM sleep, the neuromodulation level is low [86], we set g_{KL} to be a large value. In such a state, most TRN neurons are hyperpolarized and they predominantly generate strong bursting

activities with high-frequency inter-burst spikes (Figure 2A). Together with electrical couplings between neurons, the whole network generates highly synchronized responses, resulting in strong LFP (Figure 2D), and the oscillation frequency is around 4 Hz (Figure 2G), agreeing with the delta oscillation ($1-4$ Hz) observed in the experiment [87].

Light sleep condition: spindle oscillation occurs. In light sleep, i.e., N2 NREM sleep, the neuromodulation level is at the medium level [86], we set g_{KL} to be a mediate value. In this state, TRN neurons are less hyperpolarized ($-65.5 \sim -63.5$ mV) and produce weak bursts (Figure 2B). A single burst typically contains only one or two spikes, and such bursts can be easily interrupted (see the discontinuous spiking of a TRN neuron in Figure 2B). Under this condition, the whole TRN network generates oscillations of the waxing-and-waning shape (Figure 2E and SI movie **??**) with a frequency of 7 Hz (Figure 2H), which is in the range of spindle oscillation ($7-15$ Hz) [17].

We carried out ablation studies to illustrate the impact of model parameters on spindle generation. First, by removing the subcortical synaptic inputs (setting $I_{inh}=0$), the waxing-and-waning oscillation disappears in the network (see Figure S10). Second, by removing or blocking the low-threshold Ca^{2+} channel currents (setting $I_T=0$), spindle oscillation also disappears (see Figure S11). These results are in line with the experimental findings, which are: 1) the TRN slice *in vitro* without subcortical projections could not produce spindle oscillation [30]; 2) the power of spindle oscillations was significantly reduced in Ca^{2+} channel knockout mice, and the spindle rhythmogenesis in major sensory cortical areas depended on low-threshold Ca^{2+} currents [88, 89, 78].

Alertness condition. In the alertness condition, i.e., REM sleep or awake state, the neuromodulation level is high [86], we set g_{KL} to be small. In such a case, TRN neurons have depolarized resting membrane potentials (Figure 1C). Furthermore, in the REM sleep state, we set the excitatory input $I_{\text{exc}}=0$. Consistent with experimental finding [86], a significantly weak LFP signal is seen in our TRN network (Figure S6B). Moreover, TRN neurons show small voltage fluctuations and uncorrelated activities (Figure S6C) and TRN neurons under such a state present nearly no spiking activities. In the awake state, we set $I_{\text{exc}} \neq 0$ representing the excitatory input from the thalamus and cortex, and we found that TRN neurons show irregular spiking (Figure 1F) and have no dominating oscillation frequency (Figure 1I).

Phase diagram of the TRN network. In summary, Figure 1J presents how the TRN network undergoes three different states of oscillation as a function of the neuromodulation level parameter g_{KL}. As g_{KL} decreases (i.e., the neuromodulation level increases), the TRN network transitions from a regular low-frequency delta oscillation ($3-6$ Hz), to a waxing-and-waning spindle oscillation ($6-8$ Hz), and finally to irregular firings. These states correspond to the physiological states of deep sleep, light sleep, and alertness, respectively. The resting membrane potentials of individual neurons also change accordingly, rising from ($-65.5 \sim -75$mV), to ($-65.5 \sim -63.5$mV), and to (> -63.5 mV). Our model reproduces the experimental finding [39] that the resting membrane potential in spindle oscillation is more depolarized than that in delta oscillation.

Statistical properties of spindle oscillations. The experimental data has shown that spindle oscillations are characterized as $0.5-3$s long oscillation sequences in LFP which have the waxing-and-waning profile and oscillate at $7-15$ Hz [17]. The density, duration, and amplitude of spindle oscillations, all display statistical characteristics, and they are highly correlated with memory performance [90], problem-solving ability [91], and mental diseases [92]. We found that our model can reproduce the statistical properties of spindle oscillations observed in human [93, 94, 95] and animal [37, 6]. By using multichannel silicon-probe recording on the thalamus of urethane-anesthetized and sleeping rats, it was found that both the spindle oscillation cycle and the duration exhibit unimodal distributions with biases to small values (refer to the upper panels in Figure 2K and L) [6]. Consistent with these results, our network model generates spindle oscillations having similar statistical distributions (refer to the lower panels in Figure 2K and L), with the majority of spindle oscillations having $5-13$ oscillation cycles and a duration of $0.5-1.5$s. These results are also in line with the observations in human [93] and mice [37].

2.3 The mechanism of spindle generation

In the below, we further unveil the underlying mechanism of spindle generation in our TRN network. Specifically, we show that the interplay between electrical coupling and neuronal heterogeneity produces spindle oscillations.

2.3.1 Effects of electrical coupling

The role of electrical coupling in regulating TRN oscillation has been highlighted in the experiments [96, 97]. Here, we systematically investigated the effects of electrical coupling on the dynamics of the TRN network. We fixed all other parameters of the model except the conductance of electrical synapse J_e. The parameter g_{KL} reflecting neuromodulation is set to be of an intermediate value which allows the generation of spindle oscillation (see Section 2.2).

We first examined the relationship between the conductance of electrical synapse J_e and the cross-correlation (CC) among neurons in the network. As depicted in Figure S7A, we observed that CC increases as J_e rises. This phenomenon can be attributed to the synchronization of neuronal responses facilitated by electrical couplings. To further explore the impact of J_e on spindle generation, we conducted measurements and documented the probability of spindle occurrence at different J_e values (refer to Methods and Materials 4.3). The results, illustrated in Figure S7B, reveal an initial increase followed by a subsequent decrease in the probability of spindle generation with increasing J_e. This pattern suggests that an optimal electrical coupling strength is required for the spindle generation. This observation aligns with our intuition: when J_e is too small, neurons in the network fire independently, resulting in a lack of coherent oscillation in the local field potential (LFP); conversely, when J_e is too large, all neurons fire synchronously, leading to LFP oscillation at a single frequency. The subsequent sections provide a more detailed analysis of the mechanics underlying spindle generation.

We further conducted the analysis on the clustering phenomenon within the network. In this context, a cluster represents a group of interconnected neurons that fire at the same frequency. Our observations reveal that by increasing the electrical coupling conductance (J_e), the network state can be categorized into three distinct phases (Figure 3). These phases include: 1) the asynchronous firing phase (AFP, depicted in Figure 3A-C), where neuronal firings are largely independent of each other, the network lacks obvious firing clusters, and the LFP does not exhibit clear oscillation during this phase; 2) the multiple cluster phase (MCP, illustrated in Figure 3D-F), characterized by the formation of multiple clusters within the network, varying in size and oscillating at slightly different frequencies. The LFP during this phase displays spindle oscillation; 3) the synchronized firing phase (SFP, shown in Figure 3G-I), where the majority of neurons in the network synchronize their firing, resulting in the LFP oscillating at a single dominant frequency. Notably, the occurrence of spindle oscillation is specific to the MCP, and this phenomenon of multiple clustering has also been reported in a current clamp experiment conducted on the rat TRN slice [65].

2.3.2 Effects of neuronal heterogeneity

We conducted further investigation into the impact of neuronal heterogeneity on the dynamics of the TRN network. Neuronal heterogeneity, quantified by the variance of the T-type Ca^{2+} conductance (g_T) denoted as $\mathrm{Var}(g_T)$ (while keeping the mean of g_T fixed), plays a significant role in shaping the distinctive behavior of individual neurons and contributes to the desynchronization of their activities. This is evident in the decrease of cross-correlation between neurons as $\mathrm{Var}(g_T)$ increases (Figure S7C). Similarly to the effect of electrical coupling, we observed that the probability of spindle generation initially increases with $\mathrm{Var}(g_T)$ and then decreases (Figure S7D). This observation can be intuitively understood. When $\mathrm{Var}(g_T)$ is very small, neurons in the network exhibit synchronous firing, resulting in a single-frequency oscillation in the LFP. Conversely, when $\mathrm{Var}(g_T)$ is very large, neurons fire independently, leading to the absence of coherent oscillation in the LFP.

Similar to the impact of electrical coupling, the clustering phenomenon within the TRN network also undergoes three distinct phases in response to neuronal heterogeneity. However, in the case of heterogeneity, these phases appear in the reverse order as $\mathrm{Var}(g_T)$ increases, namely, SFP (Figure 3M-O), MCP (Figure 3D-F), and AFP (Figure 3J-L). The reason behind this ordering is straightforward: as the heterogeneity represented by $\mathrm{Var}(g_T)$ increases, neuronal firings become progressively more desynchronized, resulting in a transition from a single cluster to multiple clusters, and eventually to the absence of clustering. Once again, we observed that spindle oscillations occur specifically during the MCP.

In summary, our findings demonstrate that electrical coupling and neuronal heterogeneity exert contrasting effects on the dynamics of the TRN network. Electrical coupling promotes synchronization, whereas neuronal heterogeneity contributes to desynchronization. The interplay between these two factors gives rise to a diverse range of dynamics within the TRN network. Notably, when the amplitudes of electrical coupling and neuronal heterogeneity are appropriately balanced, spindle oscillation emerges. Figure 3P illustrates the phase diagram of the TRN network concerning the electrical coupling and neuronal heterogeneity.

2.3.3 Mathematical analysis of spindle generation

In the above, we have established that spindle oscillations emerge when the network state resides in the MCP. The MCP state is distinguished by the coexistence of multiple clusters with varying sizes and slightly different oscillation frequencies within the network. In the following section, we will elucidate how the MCP state gives rise to the characteristic waxing-and-waning LFP pattern.

Let us first consider two harmonic oscillators with the same amplitude but slightly different frequencies (see the example illustrated in Figure 3Q), denoted, respectively, as $y_1(t) = A\cos(2\pi\omega_1 t)$ and $y_2(t) = A\cos(2\pi\omega_2 t)$, with

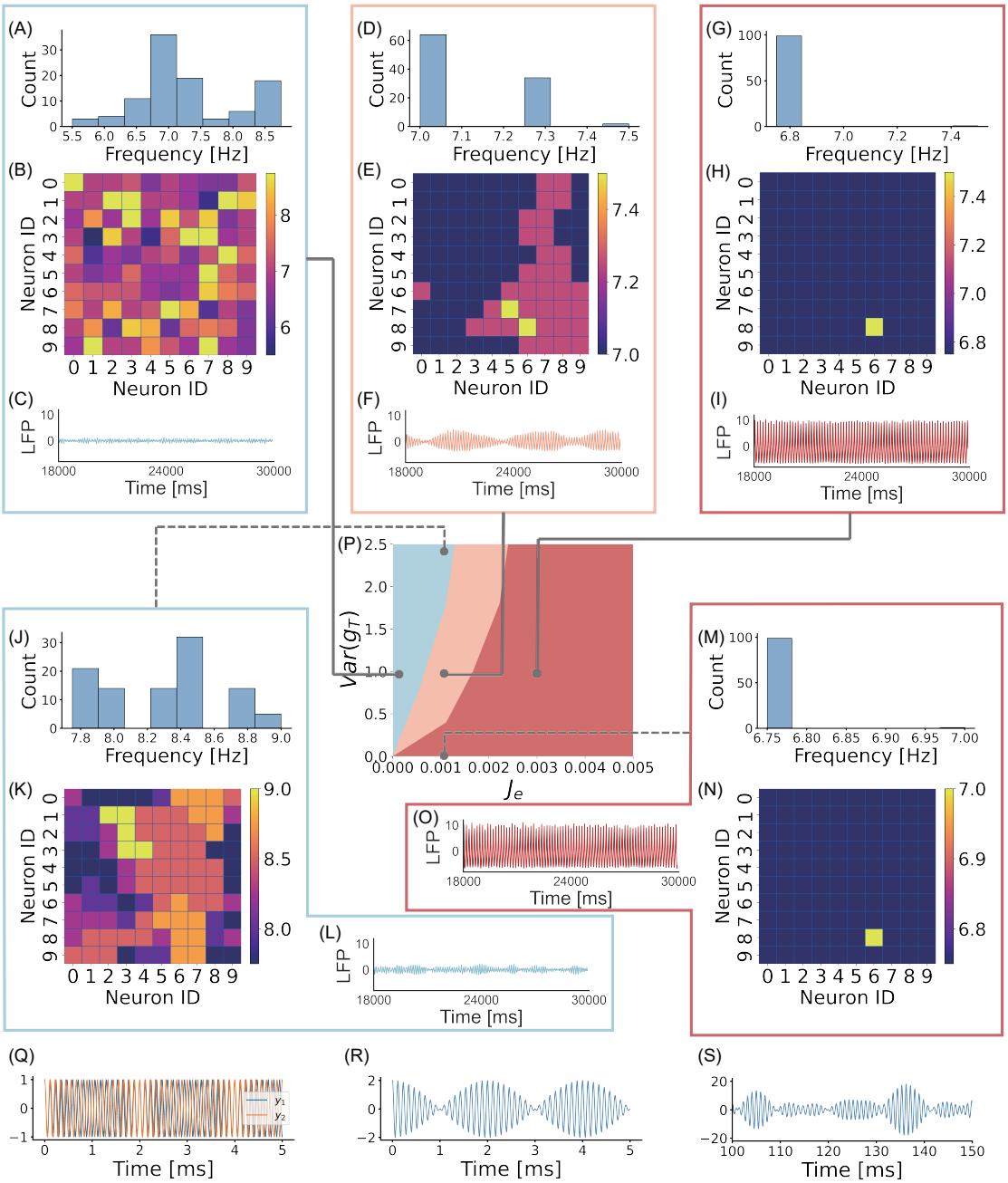

Figure 3: The mechanism of spindle generation. (A-C) Histogram of neuronal oscillation frequency, heat map of neuronal oscillation frequency, and LFP signal. The parameters are: $J_e = 0$ and $\mathrm{Var}(g_T) = 1.0$. (D-E) The same as in (A-C), except $J_e = 0.001$ and $\mathrm{Var}(g_T) = 1.0$. (G-I) The same as in (A-C), except $J_e = 0.003$ and $\mathrm{Var}(g_T) = 1.0$. (J-L) The same as in (A-C), except $J_e = 0.001$ and $\mathrm{Var}(g_T) = 2.4$. (M-N) The same as in (A-C), except $J_e = 0.001$ and $\mathrm{Var}(g_T) = 0$. (P) Phase diagram of the TRN network with respect to the electrical coupling strength J_e and the neuronal heterogeneity $\mathrm{Var}(g_T)$. (Q) Two sine waves having slightly different oscillation frequencies, where $y_1(t) = \sin(2.2\pi t)$ and $y_2(t) = \sin(2.4\pi t)$. (R) Superposition of the above two sine waves, i.e., $y(t) = y_1(t) + y_2(t)$. (S) Superposition of 100 sine waves by combining frequencies corresponding to the oscillation frequencies of TRN neurons during spindle generation.

$|\omega_1 - \omega_2| \ll (\omega_1 + \omega_2)/2$. The superposition of the two oscillators $y(t) = y_1(t) + y_2(t)$ can be expressed as

$$y(t) = 2A \cos\left[\pi\left(\omega_1 - \omega_2\right)t\right] \cos\left[\pi\left(\omega_1 + \omega_2\right)t\right]. \tag{3}$$

We see that the superposition of two oscillators displays a waxing-and-waning shaped oscillation. Specifically, the variable $y(t)$ oscillates at a high frequency of $(\omega_1 + \omega_2)/2$, while its amplitude $2A|\cos[\pi(\omega_1 - \omega_2)t]|$ oscillates at a much slower frequency of $|\omega_1 - \omega_2|$ (see Figure 3R). When considering multiple harmonic oscillators with their frequencies randomly sampled from a limited range, their superposition exhibits the characteristics of spindle oscillation. To confirm this, we extracted the oscillation frequencies of clusters in the TRN network at the MCP state (FigureS8), and used them as the frequencies of corresponding harmonic oscillators. Subsequently, we calculated the superposition of these harmonic oscillators. Our observations confirmed that the superposed activities indeed display the features of spindle oscillation, including rapid oscillation enveloped by waxing-and-waning amplitudes, as well as variations in spindle duration, amplitude, and inter-spindle interval (see FigureS8B and E). On the other hand, when we constructed harmonic oscillators using the oscillation frequencies of clusters in the phases of AFP and SFP, their superposed activities do not exhibit spindle oscillation, but rather demonstrate stochastic responses (FigureS8C and D) or regular oscillation (FigureS8A and F).

In the TRN network, we can regard a synchronized cluster as a harmonic oscillator. At the MCP state, all clusters represent distinct harmonic oscillators with slightly varying oscillation frequencies. Consequently, the collective activity of these clusters, reflected in the LFP, displays spindle oscillations, as described earlier (refer to Figure 2E and Figure 3D-F).

2.4 Spindle oscillations occur at the critical state

In the previous sections, we observed that spindle oscillations occur when the TRN network is at the MCP state, characterized by the formation of multiple synchronized clusters among the network's neurons. Interestingly, this state aligns with the critical state of a dynamical system, a common feature of complex dynamical systems [73]. The critical state is known to emerge as a result of the interplay between synchronization and desynchronization forces within the system. When the synchronization force dominates, the system exhibits high order, with only a few synchronized clusters. Conversely, when the desynchronization force dominates, the system becomes highly disordered, lacking large-size clusters. The critical state arises when these two forces are balanced, resulting in the coexistence of multiple synchronized clusters within the network. Extensive theoretical studies have highlighted the significance of criticality as the optimal condition for large systems, including neuronal networks, to process information efficiently [73].

In the TRN network, the synchronization force arises from electrical couplings between neurons, while the desynchronization force stems from neuronal heterogeneity. We have demonstrated that the interplay between these forces drives the TRN network into the MCP state, exhibiting the characteristic of criticality. In this section, we formally establish the correspondence between the MCP state and the critical state of the TRN network by computing relevant indicators of criticality.

Firstly, we examined the distribution of avalanche sizes in the TRN network. An avalanche is defined as a continuous neural response event without interruption, and its size is determined by the number of spikes within the event (see Figure 4A and Methods and Materials 4.11). Remarkably, we observed that only in the MCP state does the distribution of avalanche sizes follow a power-law pattern (Figure 4D), indicating criticality. Conversely, in other states, the power-law distribution is violated (Figure 4C and E).

Secondly, we measured the distribution of avalanche lifetimes, defined as the duration of an avalanche (Figure 4A and Methods and Materials 4.11). We found that only in the MCP state does the lifetime distribution exhibit a power-law behavior (Figure 4G), while in other states, the power-law distribution is not satisfied (Figure 4F and H).

Thirdly, we assessed the long-range temporal correlation of oscillatory signals using detrended fluctuation analysis (DFA) [98]. DFA allows us to quantify the decay rate of auto-correlations in the network fluctuation $F(w)$ (see Methods and Materials 4.11). If $F(w)$ exhibits a slowly decaying auto-correlation structure, DFA yields a power-law relationship of the form $F(w) \sim w^{\alpha}$, where $\alpha \approx 0.5$ corresponds to a disordered pattern, $0.5 < \alpha < 1$ indicates criticality, and $\alpha > 1$ reflects a highly correlated pattern. In the MCP state, we obtained $0.5 < \alpha < 1$, indicating that the network operates at the critical state (Figure 4B). Conversely, in AFR, we observed $\alpha < 0.5$, while in SFP, $\alpha > 1$ (Figure 4B), suggesting deviations from criticality.

To summarize, our findings confirm that the TRN network operates at the critical state when spindle oscillations occur. However, it is important to note that the critical state alone is insufficient to generate spindle oscillation. For instance, if we counterbalance electrical coupling with stochastic noises instead of neuronal heterogeneity, we can achieve the criticality of the network state. Nevertheless, in such cases, all clusters within the network oscillate at the same frequency, and spindle oscillation will not manifest in the LFP. In order to observe spindle oscillation, the inclusion of neuronal heterogeneity is necessary, since neuronal heterogeneity leads to that clusters oscillate at slightly different frequencies, and their superposition gives rise to the waxing-and-waning shaped oscillation (refer to the analysis in Section 2.3.3).

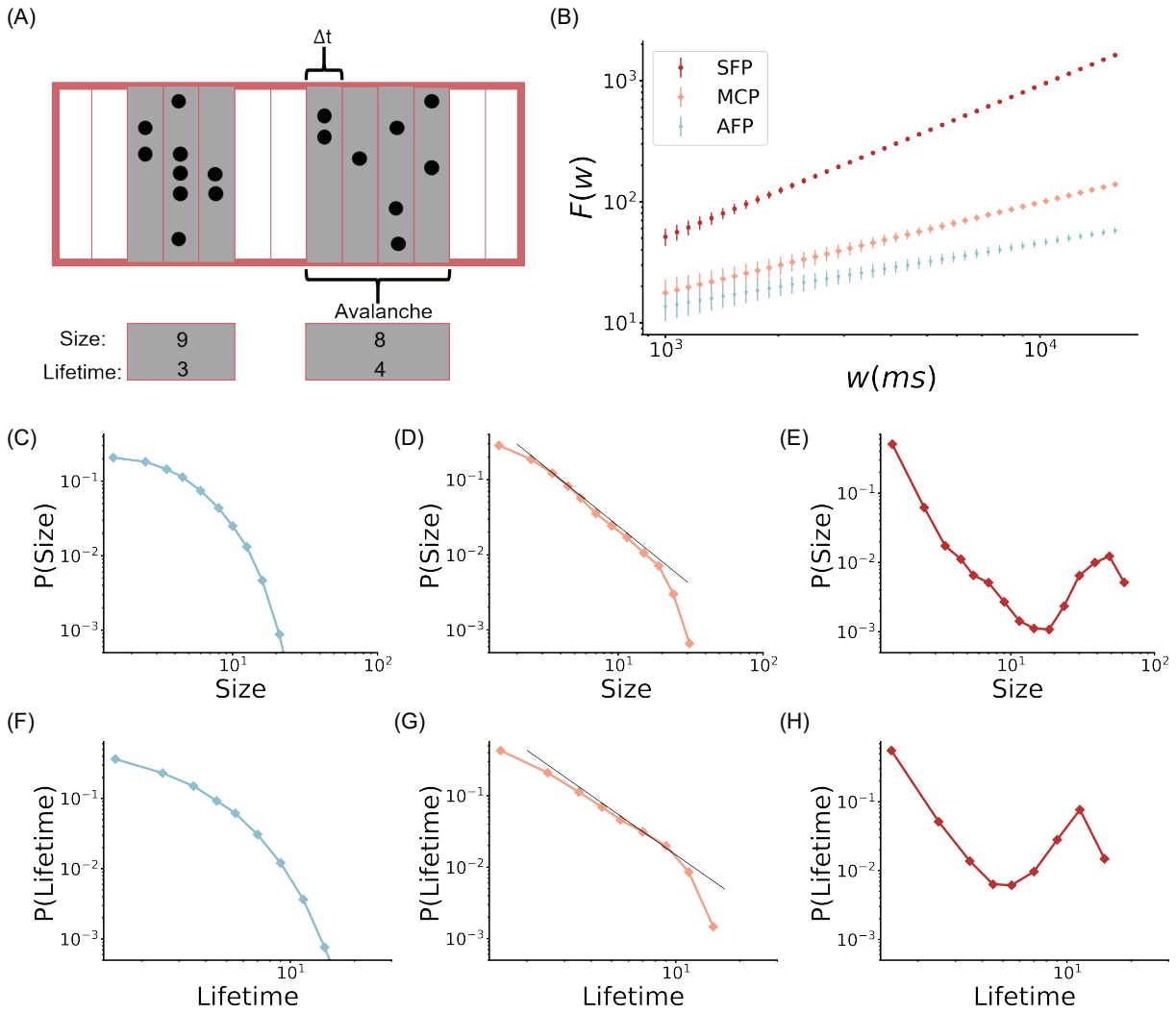

Figure 4: The critical state analysis for the spindle oscillation state. (A) The avalanche is defined as a continued response event of neurons in time (marked by gray). The size of an avalanche is the number of spikes in the event, and the lifetime is the duration of the event (measured by the number of time bins). (B) The DFA analysis for the TRN network oscillation. The x-axis represents the window width (w), while the y-axis represents the root-mean-squared fluctuation ($F(w)$) of the detrended time series of firing rate. (C-E) The log-log plot of the distribution of avalanche sizes for three different TRN states: the AFP state (C), the MCP state (D), and the SFP state (E). (F-H) The log-log plot of the distribution of avalanche lifetimes for three different TRN states: the AFP state (F), the MCP state (G), and the SFP state (H).

3 Conclusion and Discussion

The latest TRN experiments revealed that TRN neurons are highly heterogeneous and connected dominantly with electrical synapses. This challenges the classical view of spindle generation via chemical synapses in the TRN network. In this work, by building a computational model capturing the updated properties of the TRN network, we re-examined the mechanism of spindle generation. We found that the waxing-and-waning spindle oscillations naturally emerge in the TRN network as a consequence of the competition between two driving forces: electrical synapses tending to synchronize neurons while heterogeneity tending to de-synchronize neurons. The interplay between two forces drives the TRN network to fall into a state where multiple synchronized clusters with slightly different oscillation frequencies coexist. The superposition of multiple local TRN clusters thus gives rise to spindle oscillation in the recorded LFP.

Our study also revealed an interesting phenomenon regarding the activity of the TRN network during spindle oscillation, that is, the TRN network operates at the critical state. The criticality refers to a delicate balance between order and disorder in a dynamic system, where small perturbations can have profound effects on the overall behavior [73]. In the context of the TRN network, this state of criticality suggests that even subtle changes can lead to significant alterations in the network activity. This finding highlights the sensitivity of the TRN network and its crucial role in regulating spindle oscillations [16]. By operating at the critical state, the TRN network may facilitate the integration of various inputs and the coordination of neural activities across brain regions during spindle oscillations [78, 77, 99]. These insights shed new light on the intricate mechanisms underlying the generation and modulation of spindle oscillations, paving the way for further investigation into the functional significance of the criticality of spindle oscillation on the brain's learning and memory.

3.1 Experimental evidences

Our model has reproduced a number of experimental findings, including the statistical properties of the duration and the cycle number of spindle oscillations as observed in experiments [6, 93, 37]. Our model demonstrated the key roles of electrical synapses and neuronal heterogeneity in spindle generation, which are consistent with the latest experimental data. For instance, an *in vivo* experiment showed that electrical synapse blockers can effectively suppress spindle oscillation in the TRN network [100], a neurophysiological study showed that reducing the overall neuronal excitability in a TRN sector through chemogenetic inhibition can significantly decrease spindle oscillations during the NREM sleep of mice [78], and knocking out T-type Ca^{2+} channels in TC neurons (reducing heterogeneity) can reduce spindle generation in the thalamus slice [37]. Moreover, the clustered synchronized responses of TRN neurons during spindle generation were also observed in the experiment [65].

3.2 Predictions of the model

Our model produces predictions (please refer to Appendix C) that can be tested through experiments. One of our key predictions is the significant role of electrical synapses in spindle generation and regulation. To validate this prediction, we propose conducting experiments that manipulate the strength of electrical synapses and observe the corresponding effects on spindle oscillations, as predicted by our model. There are two potential methods to manipulate the amplitude of electrical coupling in the TRN. The first method involves controlling the attention level of mice. Previous studies have demonstrated that tetanic stimulation of the TRN induces long-term depression of electrical synapses between TRN neurons [101, 82]. Given the extended periods of attention processing in mice [102, 103], it can be expected that the amplitude of electrical couplings between TRN neurons decreases. By comparing the statistics of spindle oscillations at different attention levels, we can test our model's prediction. The second method entails measuring spindle oscillations in mice with knockdown of Connexin 36 (Cx36). Cx36 is the primary protein involved in the formation of gap junctions in the TRN [65, 67]. Our model predicts that spindle oscillations in Cx36 knockdown mice are impaired compared to wild-type mice.

3.3 Limitations of the model

While our model successfully demonstrates the generation of spindle oscillations in an electrically coupled heterogeneous TRN network, there are several areas that require further investigation. Firstly, it is important to note that the TRN network is a component of the broader cortico-thalamic circuit, receiving excitatory projections from thalamic and cortical regions, as well as substantial inhibitory innervation from subcortical areas. In this study, we primarily focused on the contribution of synaptic projections from subcortical areas in generating spindle oscillations. However, numerous studies have highlighted the involvement of interactions between the thalamus and cortex in spindle initiation, oscillation, and termination [16]. Future research will involve expanding our current model to incorporate the influence of cortical inputs. Secondly, it is worth noting that electrical synapses between TRN neurons have been reported to exhibit plasticity and asymmetry [101, 82, 104]. Their activity-dependent plasticity has been hypothesized to play a significant role in TRN network oscillation [97]. However, our present study neglects the dynamic properties of electrical synapses. In future work, we plan to extend our current model to investigate the roles of plasticity and asymmetry in spindle generation.

3.4 The multifaceted origin of spindle generation

The traditional perspective suggests that spindle oscillations primarily originate from the thalamus, as supported by evidence in animal experiments, in which the persistence of spindle activity in the thalamus even when the cortex is completely removed [105, 2, 106]. However, recent experimental findings have challenged this perspective, proposing that spindle oscillations may have diverse origins within the brain [32]. Firstly, optogenetic stimulation of the TRN

has been shown to induce cortical spindle activities that are not observed in corresponding thalamic sites [36]. This suggests that the TRN may play a role in initiating spindle oscillations. Secondly, EEG and MEG recordings have led to the hypothesis that EEG spindles are generated by matrix (nonspecific) thalamic nuclei, while MEG spindles are generated by core (specific) thalamic pathways [107, 108, 109]. This indicates that different thalamic regions may contribute to distinct types of spindle oscillations. Additionally, a recent human study suggests that Na^{+} and Ca^{2+} antagonists have varying effects on fast and slow spindles [110]. Specifically, the administration of the Ca^{2+} channel blocker diminishes only fast spindles. These findings further support the idea that spindle oscillations can originate from different mechanisms. In our model, although we focus on an electrically coupled, heterogeneous TRN network, we demonstrate that the criticality of the network state is crucial for generating spindle oscillations. When a neural circuit reaches this critical state and exhibits neuronal heterogeneity, it possesses the potential to generate spindle oscillations. By recognizing the ubiquity of criticality in the brain [73], our model provides novel insights into the emergence of spindle oscillations across diverse brain regions.

4 Methods and Materials

4.1 Network structure

To mimic a $1 \times 1\,\mathrm{mm}$ of TRN slice, we modeled a tier of TRN network which contains 100 (10×10) neurons (see Figure 1A). The TRN network is placed in a two-dimensional grid with a periodic boundary, in which neurons are electrically coupled with each other by a Gaussian probability connection pattern. The connection probability for each pair of neurons (i, j) obeys

$$p_{i,j} = G(d_{ij}), \tag{4}$$

where d_{ij} is the Euclidean distance between two neurons, and G is a 2-dimensional Gaussian function centered at 0 with the standard deviation σ, and σ controls the connection width of each neuron.

In addition to the electrical couplings between neurons, each neuron may receive two other kinds of synaptic projections (see Figure 1A). To mimic the physiological condition of the TRN network in *vivo*, a neuron receives the inhibitory projections from the subcortical structures [51, 52, 111]. This inhibitory projection is modeled as a train of Poisson spikes conveying currents onto the neuron with $\mathrm{GABA_A}$ synapse (see Methods and Materials 4.4). To model the synaptic connections from the thalamus and cortex in the awake state, a neuron receives a spike train with excitatory AMPA synapse (see Methods and Materials 4.5). Particularly, the firing rates of both excitatory and inhibitory background inputs used in our model are 50 Hz.

4.2 TRN neuron model

For the convenience of analysis, we used the previously developed reduced TRN neuron model [75]. It is biologically grounded, capable of reproducing characteristic TRN bursts and tonic discharges (see Appendix A), and allows easy dynamical analysis.

Specifically, the TRN neuron is modeled as a single-compartment Hodgkin-Huxley model, with a minimal set of active channels that are sufficient to produce the tonic and bursting spiking dynamics. It contains three active ionic currents: a fast sodium current (I_{Na}) and a delayed rectifier (I_K) for spiking generation and a low-threshold Ca^{2+} current (I_T) for rebound bursting. Moreover, it has two passive leaky channels: a potassium leaky current (I_{KL}) for modeling the neuromodulation effect, and a leaky current (I_L).

The dynamics of the TRN neuron model is given by

$$\begin{aligned}\tau\frac{dV}{dt} =& \underbrace{g_{Na}m_\infty^3(V)h_\infty(y)(E_{Na}-V)}_{I_{Na}} + \underbrace{g_T p_\infty^2(y)q_\infty(z)(E_T-V)}_{I_T} \\ &+ \underbrace{g_K n_\infty^4(y)(E_K-V)}_{I_K} + \underbrace{g_L(E_L-V)}_{I_L} + \underbrace{g_{KL}(E_{KL}-V)}_{I_{KL}} + \frac{10^{-3}}{A}I_{syn}(t),\end{aligned} \tag{5a}$$

$$\frac{dy}{dt} = \phi_h\rho_h\frac{h_\infty(V)-h_\infty(y)}{\tau_h(V)h'_\infty(y)} + \phi_n\rho_n\frac{n_\infty(V)-n_\infty(y)}{\tau_n(V)n'_\infty(y)} + \phi_p\rho_p\frac{p_\infty(V)-p_\infty(y)}{\tau_p(V)p'_\infty(y)}, \tag{5b}$$

$$\frac{dz}{dt} = \phi_q\frac{q_\infty(V)-q_\infty(z)}{\tau_q(V)q'_\infty(z)}, \tag{5c}$$

where $\tau = C/\rho_V$ is the membrane time constant, I_{syn} is the received synaptic current that normalized by the membrane area $A = 1.43 \times 10^{-4}\,\mathrm{cm}^2$, I_{Na}, I_K and I_T are the currents mediated by the sodium, potassium and low-threshold calcium channels, respectively, I_L is the leakage current, I_{KL} is the potassium leaky current controlled by neuromodulators like acetylcholine and norepinephrine, $C = 1\,\mu\mathrm{F/cm}^2$ is the membrane capacitance, ρ_V is the reduction coefficient of the membrane potential V [75], y and z are two reduced equivalent potentials [75], ρ_h, ρ_n and ρ_p are reduction coefficients [75], $\phi_h = 1, \phi_n = 1, \phi_p = 6.9$ and $\phi_q = 3.7$ are temperature factors, $\tau_x(x \in \{h, n, p, q\})$ are time constant functions of each variable, and $x_\infty(x \in \{h, n, p, q\})$ are steady-state functions. The detail expressions of reduction coefficients (including $\rho_V, \rho_h, \rho_n, \rho_p, \rho_q$), time constant functions (including $\tau_h, \tau_n, \tau_p, \tau_q$), and steady-state functions (including $h_\infty, n_\infty, p_\infty, q_\infty$) can be obtained in [75].

For the sodium current I_{Na}, we set the maximal conductance $g_{Na} = 100\,\mathrm{mS/cm}^2$, the reversal potential $E_{Na} = 50\,\mathrm{mV}$, and the spike adjusting threshold $V_{th}^{Na} = -55\,\mathrm{mV}$. For the potassium current I_K, we set $V_{th}^K = -55\,\mathrm{mV}$, $E_K = -100\,\mathrm{mV}$, and $g_K = 10\,\mathrm{mS/cm}^2$. For the low-threshold calcium current I_T, we set $g_T = 2.25\,\mathrm{mS/cm}^2$, and $V_{th}^T = -3\,\mathrm{mV}$. For the leakage current I_L, we used the leakage channel conductance $g_L = 0.06\,\mathrm{mS/cm}^2$ and the

leakage reversal potential $E_L = -70\,\mathrm{mV}$. For the potassium leaky current I_{KL}, we set the potassium leakage channel conductance $g_{KL} = 0.0065\,\mathrm{mS/cm^2}$ and the reversal potential $E_{KL} = -100\,\mathrm{mV}$.

The synaptic current of the TRN neuron i is decomposed into three components:

$$I^i_{syn}(t) = I^i_{gap}(t) + I^i_{inh}(t) + I^i_{exc}(t), \tag{6}$$

where I_{gap} is the electrical synapse current (see Methods and Materials 4.3), I_{inh} the inhibitory GABA$_A$ current (see Methods and Materials 4.4), and I_{exc} the excitatory AMPA current (see Methods and Materials 4.5). They are described in the following.

4.3 Electrical synapse model

The electrical synapse current flowing into the TRN neuron i is computed as

$$I^i_{gap} = \sum_{j \in N_{gj}(i)} J_e(V_j - V_i), \tag{7}$$

where J_e is the conductance of electrical synapses, and $N_{gj}(i)$ denotes the collection of neurons that are electrically coupled with the neuron i.

4.4 Subcortical inhibitory synapse model

The inhibitory synaptic current I^i_{inh} to the neuron i from the transmission of a subcortical spike is computed as the GABA$_A$ synapse model. Specifically, it is modeled as:

$$I^i_{inh} = \overline{g}_{GABA_A} \cdot s \cdot (V_i - E_{GABA_A}), \tag{8}$$

where $\overline{g}_{GABA_A}$ denotes the maximum GABA$_A$ synaptic conductance, E_{GABA_A} the synaptic reversal potential, and s the fraction of open channels. Moreover, s is modeled by the first-order activation scheme

$$\frac{\mathrm{d}s}{\mathrm{d}t} = \alpha[T](1-s) - \beta s, \tag{9}$$

where $[T]$ is the concentration of neurotransmitter modeled as a brief pulse (0.3 ms duration, 0.5 mM amplitude) after pre-synaptic neuron generating an action potential [35], and α and β are the channel forward and backward binding rates given by $\alpha = 10\,\mathrm{ms}^{-1}$ and $\beta = 0.18\,\mathrm{ms}^{-1}$, respectively [35, 112, 113].

4.5 Thalamic and cortical excitatory synapse model

The excitatory synaptic current I^i_{exc} to the neuron i when receiving a thalamic or cortical spike is computed as the AMPA synapse model. Specifically, the AMAP current is modeled as

$$I^i_{exc} = \overline{g}_{AMPA} \cdot s \cdot (V_i - E_{AMPA}), \tag{10}$$

where $\overline{g}_{AMPA}$ denotes the maximum AMPA synaptic conductance, and E_{AMPA} the synaptic reversal potential. Similar to GABA$_A$ model, s is modeled by Eq. 9, except that $\alpha = 10.5\,\mathrm{ms}^{-1}$ and $\beta = 0.166\,\mathrm{ms}^{-1}$ [35, 112, 113].

4.6 Simulation tool

The network model was coded with the BrainPy library in Python [114, 115]. All simulations were performed by using the fourth-order Runge-Kutta method (RK4) with a fixed time step of 0.01 ms. A shorter simulation time step does not change the results. The model source code is available on the GitHub.

4.7 Local field potential

We measured the local field potential by averaging the membrane potentials across the whole TRN neuron group, which is written as,

$$\mathrm{LFP} = \frac{\sum_i^N V_i}{N}. \tag{11}$$

We then used a finite impulse response (FIR) filter (`mne.filter.filter_data()`, a built-in function implemented in MNE-Python toolbox [116]) to calculate the broadband filtered LFP signal (0.5 $\sim$ 30 Hz) $\mathrm{LFP_{bf}}$ and the spindle band filtered signal (6 $\sim$ 10 Hz) $\mathrm{LFP_{spin}}$. The power spectrum of the LFP was obtained by a fast Fourier transform (FFT) on $\mathrm{LFP_{bf}}$. The peak spectral frequency was chosen as the network oscillation frequency.

4.8 Automatic spindle detection

Spindles are automatically detected, with the method inspired by the A7 algorithm described in [117] and the YASA spindle algorithm presented in [118]. Specifically, four thresholds are used:

Relative spindle power $\mathrm{RelSpinPow}$

The first threshold is computed as the relative power in the spindle frequency range, which aims to ensure the increase of the power is specific to the spindle oscillation range and not due to a global oscillation power increase. The threshold is set to $\mathrm{RelSpinPow} \geq 0.9$.

Root mean square RMS

In order to detect the energy power increase in the spindle frequency band, the moving RMS of $\mathrm{LFP}_{\mathrm{spin}}$ with a window size of 100 ms and a step size of 50 ms is calculated. The threshold is exceeded whenever a sample has a $\mathrm{RMS} \geq \mathrm{RMS}_{\mathrm{threshold}}$, where $\mathrm{RMS}_{\mathrm{threshold}} = \mathrm{RMS}_{\mathrm{mean}} + 0.1\mathrm{RMS}_{\mathrm{std}}$.

Spindle correlation $\mathrm{SpinCorr}$

In order to characterize the causal influence of $\mathrm{LFP}_{\mathrm{spin}}$ power increase on $\mathrm{LFP}_{\mathrm{bf}}$ rise, $\mathrm{SpinCorr}$ is computed by the Pearson correlation coefficient between $\mathrm{LFP}_{\mathrm{spin}}$ and $\mathrm{LFP}_{\mathrm{bf}}$ with a moving sliding window of 300 ms and a step of 100 ms. The threshold is exceeded whenever a sample has a correlation value $\mathrm{SpinCorr} \geq 0.9$.

Gaussian kernel fitting errors err_p

When the above three parameters exceed their respective thresholds, a candidate spindle event can be selected. However, the morphologies of such events extracted by three thresholds may not be waxing and waning. Therefore, we fit the cycle peaks in each spindle candidate with a Gaussian kernel $f(x, \mu, \sigma, A) = \frac{A}{\sigma\sqrt{2\pi}} \exp\left(-\frac{(x-\mu)^2}{2\sigma^2}\right)$ to filter out the false alarm event. The standard deviation errors (err_p) on the parameters ($p \in \{A, \mu, \sigma\}$) after curve fitting are used for the threshold judgment. Once one of the errors exceeds 10., we will reject this candidate event.

4.9 Cross correlation

The cross-correlation between a pair of neurons is calculated as follows. After denoting the spike trains of a pair of neurons to be $S_i(t)$ and $S_j(t)$, for $S_i(t), S_j(t) = 0$ or 1, and $t = 1, 2, ..., T$, the CC between the neuron pair is calculated to be

$$CC_{ij} = \frac{\sum_{t=1}^{T} S_i(t) S_j(t)}{\sqrt{\sum_{t=1}^{T} S_i(t)}\sqrt{\sum_{t=1}^{T} S_j(t)}}. \tag{12}$$

For a network, the overall cross-correlation is given by,

$$CC = \frac{\sum_{i,j(i\neq j)}^{N} CC_{ij}}{N(N-1)/2}, \tag{13}$$

where the summation runs over all neuron pairs.

4.10 Coupling coefficient

To assess the strength of the electrical synapse connection, we utilized the steady-state coupling coefficient (CC) as a measure. This involved injecting long polarizing current pulses into one of the paired neurons. The injection of current induced a voltage drop in the presynaptic cell ($\mathrm{V}_{\mathrm{pre}}$), which typically caused a change in the membrane potential of the coupled postsynaptic cell ($\mathrm{V}_{\mathrm{post}}$). The duration of the current pulses was intentionally extended to overcome the initial attenuation of the membrane potential caused by the passive properties of the postsynaptic membrane's filtering characteristics. Consequently, we were able to measure voltage changes in a stable state. Quantitatively, the strength of coupling was determined by calculating the coupling coefficient, defined as the ratio between the voltage deflections observed in the post- and presynaptic cells:

$$\mathrm{CC} = \frac{\mathrm{V}_{\mathrm{post}}}{\mathrm{V}_{\mathrm{pre}}}$$

4.11 Critical state analysis

In accordance with the classical analysis of criticality in spiking activity [119], we quantified the number of spikes in each bin, which has a length of Δt, for the merged spike trains. An avalanche is defined as a consecutive sequence of bins, separated by a silent period. In this study, we defined the size of an avalanche, denoted as S, as the total number of spikes it contains, and the lifetime, denoted as T, as the number of bins it spans. Generally, we selected the average inter-spike interval of the merged spiking train as the bin length, Δt.

We began by visually inspecting the distributions of avalanche size and lifetime. For distributions that exhibit characteristics of the power law, we employed a doubly truncated algorithm based on the maximum likelihood estimation [120, 121] to analyze them. We fit a discrete power-law distribution

$$f(x) = \frac{1}{\sum_{x=x_{\min}}^{x_{\max}} \left(\frac{1}{x}\right)^{\alpha}} \left(\frac{1}{x}\right)^{\alpha}, \tag{14}$$

where $x_{\min}$ is the smallest observable size or lifetime, and the upper bound $x_{\max}$ is different for different datasets. We estimated α by maximizing the likelihood function

$$L(\alpha) = \prod_{i=1}^{N} f\left(x_i\right), \tag{15}$$

where N is the number of measurements.

To assess the goodness of fit and determine if a power law adequately describes the data, we employed several evaluation techniques [122]. First, we employed bootstrapping and the Kolmogorov-Smirnov test to generate a p-value for an individual fit. Second, we utilized the log-likelihood ratio to compare two fits and identified the better one. The p-value obtained from the Kolmogorov-Smirnov test represents the significance level of the fit. By comparing the log-likelihood ratio between two candidate distributions, we can determine if the data is more likely to follow one distribution over the other. A positive log-likelihood ratio indicates that the data is more likely to adhere to the first distribution, while a negative value suggests a greater likelihood for the second distribution [122].

In order to analyze the scale-invariant long-range time correlation, we employed detrended fluctuation analysis (DFA) [98]. This method involves several steps. Initially, we obtained an integrated zero-mean version of the original time series z, denoted as $y(k)$, by summing the deviations from the mean $z(i)$ up to the k-th point, i.e., $y(k) = \sum_{i=1}^{k}[z(i) - \langle z \rangle]$. Next, we divided the entire time period into consecutive non-overlapping bins of width w and fit a local linear trend, denoted as y_w, to each bin. Finally, we calculated the fluctuation $F(w)$ at a given time-scale w using the following equation:

$$F(w) = \sqrt{\frac{1}{N}\sum_{i=1}^{N}\left[y(i) - y_w(i)\right]^2}, \tag{16}$$

where N is the total number of time windows.

5 Data Availability

All datasets generated for this study are included in the article/Appendix. For the detailed parameter setting, please refer to the ref. [75]. The source code to reproduce the model is available on GitHub: `https://github.com/shangyangli/TRN-spindle`

References

[1] Brittany C Clawson, Jaclyn Durkin, and Sara J Aton. Form and function of sleep spindles across the lifespan. *Neural plasticity*, 2016.

[2] M Steriade, M Deschenes, L Domich, and C Mulle. Abolition of spindle oscillations in thalamic neurons disconnected from nucleus reticularis thalami. *Journal of neurophysiology*, 54(6):1473–1497, 1985.

[3] M Steriade, L Domich, G Oakson, and M Deschenes. The deafferented reticular thalamic nucleus generates spindle rhythmicity. *Journal of neurophysiology*, 57(1):260–273, 1987.

[4] Stephen Thankachan, Fumi Katsuki, James T McKenna, Chun Yang, Charu Shukla, Karl Deisseroth, David S Uygun, Robert E Strecker, Ritchie E Brown, James M McNally, et al. Thalamic reticular nucleus parvalbumin neurons regulate sleep spindles and electrophysiological aspects of schizophrenia in mice. *Scientific reports*, 9(1):1–16, 2019.

[5] Michael M Halassa, Zhe Chen, Ralf D Wimmer, Philip M Brunetti, Shengli Zhao, Basilis Zikopoulos, Fan Wang, Emery N Brown, and Matthew A Wilson. State-dependent architecture of thalamic reticular subnetworks. *Cell*, 158(4):808–821, 2014.

[6] Péter Barthó, Andrea Slézia, Ferenc Mátyás, Lejla Faradzs-Zade, István Ulbert, Kenneth D Harris, and László Acsády. Ongoing network state controls the length of sleep spindles via inhibitory activity. *Neuron*, 82(6):1367–1379, 2014.

[7] Oxana Eschenko, Matthias Mölle, Jan Born, and Susan J Sara. Elevated sleep spindle density after learning or after retrieval in rats. *Journal of Neuroscience*, 26(50):12914–12920, 2006.

[8] Thierry Bal, Marcus von Krosigk, and David A McCormick. Synaptic and membrane mechanisms underlying synchronized oscillations in the ferret lateral geniculate nucleus in vitro. *The Journal of physiology*, 483(3):641–663, 1995.

[9] Uhnoh Kim, Thierry Bal, and David A McCormick. Spindle waves are propagating synchronized oscillations in the ferret lgnd in vitro. *Journal of Neurophysiology*, 74(3):1301–1323, 1995.

[10] Ivaylo Borislavov Iotchev, Vivien Reicher, Enikő Kovács, Tímea Kovács, Anna Kis, Márta Gácsi, and Enikő Kubinyi. Averaging sleep spindle occurrence in dogs predicts learning performance better than single measures. *Scientific Reports*, 10(1):1–6, 2020.

[11] Róbert Bódizs, Anna Kis, Márta Gácsi, and József Topál. Sleep in the dog: comparative, behavioral and translational relevance. *Current Opinion in Behavioral Sciences*, 33:25–33, 2020.

[12] Will T Schneider, Szilvia Vas, Alister U Nicol, and A Jennifer Morton. Characterizing sleep spindles in sheep. *Eneuro*, 7(2), 2020.

[13] Saori Takeuchi, Rie Murai, Hideki Shimazu, Yoshikazu Isomura, Tatsuya Mima, and Toru Tsujimoto. Spatiotemporal organization and cross-frequency coupling of sleep spindles in primate cerebral cortex. *Sleep*, 39(9):1719–1735, 2016.

[14] Srihari Y Sritharan, Enrique Contreras-Hernández, Andrew G Richardson, and Timothy H Lucas. Primate somatosensory cortical neurons are entrained to both spontaneous and peripherally evoked spindle oscillations. *Journal of neurophysiology*, 123(1):300–307, 2020.

[15] Alered L Loomis, E Newton Harvey, and Garret Hobart. Potential rhythms of the cerebral cortex during sleep. *Science*, 1935.

[16] Laura MJ Fernandez and Anita Lüthi. Sleep spindles: mechanisms and functions. *Physiological reviews*, 100(2):805–868, 2020.

[17] Adrien Peyrache and Julie Seibt. A mechanism for learning with sleep spindles. *Philosophical Transactions of the Royal Society B*, 375(1799):20190230, 2020.

[18] Steffen Gais, Matthias Mölle, Kay Helms, and Jan Born. Learning-dependent increases in sleep spindle density. *Journal of Neuroscience*, 22(15):6830–6834, 2002.

[19] Manuel Schabus, Georg Gruber, Silvia Parapatics, Cornelia Sauter, Gerhard Klösch, Peter Anderer, Wolfgang Klimesch, Bernd Saletu, and Josef Zeitlhofer. Sleep spindles and their significance for declarative memory consolidation. *Sleep*, 27(8):1479–1485, 2004.

[20] Zofia Clemens, Daniel Fabó, and Peter Halász. Overnight verbal memory retention correlates with the number of sleep spindles. *Neuroscience*, 132(2):529–535, 2005.

[21] Marc Barakat, Julie Carrier, Karen Debas, Ovidiu Lungu, Stuart Fogel, Gilles Vandewalle, Richard D Hoge, Pierre Bellec, Avi Karni, Leslie G Ungerleider, et al. Sleep spindles predict neural and behavioral changes in motor sequence consolidation. *Human brain mapping*, 34(11):2918–2928, 2013.

[22] Samuel Laventure, Stuart Fogel, Ovidiu Lungu, Geneviève Albouy, Pénélope Sévigny-Dupont, Catherine Vien, Chadi Sayour, Julie Carrier, Habib Benali, and Julien Doyon. Nrem2 and sleep spindles are instrumental to the consolidation of motor sequence memories. *PLoS biology*, 14(3):e1002429, 2016.

[23] Lisa Marshall, Halla Helgadóttir, Matthias Mölle, and Jan Born. Boosting slow oscillations during sleep potentiates memory. *Nature*, 444(7119):610–613, 2006.

[24] Caroline Lustenberger, Michael R Boyle, Sankaraleengam Alagapan, Juliann M Mellin, Bradley V Vaughn, and Flavio Fröhlich. Feedback-controlled transcranial alternating current stimulation reveals a functional role of sleep spindles in motor memory consolidation. *Current Biology*, 26(16):2127–2136, 2016.

[25] P Michelle Fogerson and John R Huguenard. Tapping the brakes: cellular and synaptic mechanisms that regulate thalamic oscillations. *Neuron*, 92(4):687–704, 2016.

[26] RS Morison and DL Bassett. Electrical activity of the thalamus and basal ganglia in decorticate cats. *Journal of Neurophysiology*, 8(5):309–314, 1945.

[27] I Timofeev and M Steriade. Low-frequency rhythms in the thalamus of intact-cortex and decorticated cats. *Journal of neurophysiology*, 76(6):4152–4168, 1996.

[28] JR Huguenard and DA Prince. Intrathalamic rhythmicity studied in vitro: nominal t-current modulation causes robust antioscillatory effects. *Journal of Neuroscience*, 14(9):5485–5502, 1994.

[29] RICHARD A Warren, ARIEL Agmon, and EDWARD G Jones. Oscillatory synaptic interactions between ventroposterior and reticular neurons in mouse thalamus in vitro. *Journal of Neurophysiology*, 72(4):1993–2003, 1994.

[30] M von Krosigk, Thierry Bal, and David A. McCormick. Cellular mechanisms of a synchronized oscillation in the thalamus. *Science*, 261 5119:361–4, 1993.

[31] Thierry Bal, Marcus von Krosigk, and David A McCormick. Role of the ferret perigeniculate nucleus in the generation of synchronized oscillations in vitro. *The Journal of physiology*, 483(3):665–685, 1995.

[32] Igor Timofeev and Sylvain Chauvette. The spindles: are they still thalamic?, 2013.

[33] David Golomb, Xiao-Jing Wang, and John Rinzel. Synchronization properties of spindle oscillations in a thalamic reticular nucleus model. *Journal of neurophysiology*, 72(3):1109–1126, 1994.

[34] XJ Wang, D Golomb, and J Rinzel. Emergent spindle oscillations and intermittent burst firing in a thalamic model: specific neuronal mechanisms. *Proceedings of the National Academy of Sciences*, 92(12):5577–5581, 1995.

[35] Alain Destexhe, Thierry Bal, David A McCormick, and Terrence J Sejnowski. Ionic mechanisms underlying synchronized oscillations and propagating waves in a model of ferret thalamic slices. *Journal of neurophysiology*, 76(3):2049–2070, 1996.

[36] Michael M Halassa, Joshua H Siegle, Jason T Ritt, Jonathan T Ting, Guoping Feng, and Christopher I Moore. Selective optical drive of thalamic reticular nucleus generates thalamic bursts and cortical spindles. *Nature neuroscience*, 14(9):1118–1120, 2011.

[37] Jungryun Lee, Kiyeong Song, Kyoobin Lee, Joohyeon Hong, Hyojung Lee, Sangmi Chae, Eunji Cheong, and Hee-Sup Shin. Sleep spindles are generated in the absence of t-type calcium channel-mediated low-threshold burst firing of thalamocortical neurons. *Proceedings of the National Academy of Sciences*, 110(50):20266–20271, 2013.

[38] Amr Ayoub, Dominic Aumann, Anne Hörschelmann, Atossa Kouchekmanesch, Pia Paul, Jan Born, and Lisa Marshall. Differential effects on fast and slow spindle activity, and the sleep slow oscillation in humans with carbamazepine and flunarizine to antagonize voltage-dependent na+ and ca2+ channel activity. *Sleep*, 36(6):905–911, 2013.

[39] D Contreras, R Curró Dossi, and M Steriade. Electrophysiological properties of cat reticular thalamic neurones in vivo. *The Journal of Physiology*, 470(1):273–294, 1993.

[40] Pablo Fuentealba and Mircea Steriade. The reticular nucleus revisited: intrinsic and network properties of a thalamic pacemaker. *Progress in neurobiology*, 75(2):125–141, 2005.

[41] D Pinault. The thalamic reticular nucleus: structure, function and concept. *Brain Research Reviews*, 46:1–31, 2004.

[42] Michael M Halassa and László Acsády. Thalamic inhibition: diverse sources, diverse scales. *Trends in neurosciences*, 39(10):680–693, 2016.

[43] John W Crabtree. Functional diversity of thalamic reticular subnetworks. *Frontiers in systems neuroscience*, 12:41, 2018.

[44] Chisato Asanuma. Axonal arborizations of a magnocellular basal nucleus input and their relation to the neurons in the thalamic reticular nucleus of rats. *Proceedings of the National Academy of Sciences*, 86(12):4746–4750, 1989.

[45] C Asanuma and LL Porter. Light and electron microscopic evidence for a gabaergic projection from the caudal basal forebrain to the thalamic reticular nucleus in rats. *Journal of comparative neurology*, 302(1):159–172, 1990.

[46] ME Bickford, AE Günlük, SC Van Horn, and SM Sherman. Gabaergic projection from the basal forebrain to the visual sector of the thalamic reticular nucleus in the cat. *Journal of Comparative Neurology*, 348(4):481–510, 1994.

[47] Yan-Gang Sun, Vanessa Rupprecht, Li Zhou, Rajan Dasgupta, Frederik Seibt, and Michael Beierlein. mglur1 and mglur5 synergistically control cholinergic synaptic transmission in the thalamic reticular nucleus. *Journal of Neuroscience*, 36(30):7886–7896, 2016.

[48] D Paré, L-N Hazrati, A Parent, and M Steriade. Substantia nigra pars reticulata projects to the reticular thalamic nucleus of the cat: a morphological and electrophysiological study. *Brain research*, 535(1):139–146, 1990.

[49] Lili-Naz Hazrati et al. Projection from the external pallidum to the reticular thalamic nucleus in the squirrel monkey. *Brain research*, 550(1):142–146, 1991.

[50] C Asanuma. Gabaergic and pallidal terminals in the thalamic reticular nucleus of squirrel monkeys. *Experimental brain research*, 101(3):439–451, 1994.

[51] Gubbi Govindaiah, Tongfei Wang, Martha U Gillette, Shane R Crandall, and Charles L Cox. Regulation of inhibitory synapses by presynaptic d4 dopamine receptors in thalamus. *Journal of neurophysiology*, 104(5):2757–2765, 2010.

[52] Carolina Gutierrez Herrera, Marta Carus Cadavieco, Sonia Jego, Alexey Ponomarenko, Tatiana Korotkova, and Antoine Adamantidis. Hypothalamic feedforward inhibition of thalamocortical network controls arousal and consciousness. *Nature neuroscience*, 19(2):290–298, 2016.

[53] Gunilla Ahlsén and Sivert Lindström. Mutal inhibition between perigeniculate neurones. *Brain research*, 236(2):482–486, 1982.

[54] Maria V Sanchez-Vives, Thierry Bal, and David A McCormick. Inhibitory interactions between perigeniculate gabaergic neurons. *Journal of Neuroscience*, 17(22):8894–8908, 1997.

[55] Yousheng Shu and David A McCormick. Inhibitory interactions between ferret thalamic reticular neurons. *Journal of Neurophysiology*, 87(5):2571–2576, 2002.

[56] Charlotte Deleuze and John R Huguenard. Distinct electrical and chemical connectivity maps in the thalamic reticular nucleus: potential roles in synchronization and sensation. *Journal of Neuroscience*, 26(33):8633–8645, 2006.

[57] Ying-Wan Lam, Christopher S Nelson, and S Murray Sherman. Mapping of the functional interconnections between thalamic reticular neurons using photostimulation. *Journal of neurophysiology*, 96(5):2593–2600, 2006.

[58] X-J Wang and J Rinzel. Spindle rhythmicity in the reticularis thalami nucleus: synchronization among mutually inhibitory neurons. *Neuroscience*, 53(4):899–904, 1993.

[59] Alain Destexhe, Diego Contreras, Terrence J Sejnowski, and Mircea Steriade. A model of spindle rhythmicity in the isolated thalamic reticular nucleus. *Journal of neurophysiology*, 72(2):803–818, 1994.

[60] M Bazhenov, I Timofeev, M Steriade, and TJ Sejnowski. Self–sustained rhythmic activity in the thalamic reticular nucleus mediated by depolarizing gaba a receptor potentials. *Nature neuroscience*, 2(2):168–174, 1999.

[61] Daniel Ulrich and John R Huguenard. Nucleus-specific chloride homeostasis in rat thalamus. *Journal of Neuroscience*, 17(7):2348–2354, 1997.

[62] Yan-Gang Sun, Chia-Shan Wu, John J Renger, Victor N Uebele, Hui-Chen Lu, and Michael Beierlein. Gabaergic synaptic transmission triggers action potentials in thalamic reticular nucleus neurons. *Journal of Neuroscience*, 32(23):7782–7790, 2012.

[63] Peter M Klein, Adam C Lu, Megan E Harper, Hannah M McKown, Jessica D Morgan, and Mark P Beenhakker. Tenuous inhibitory gabaergic signaling in the reticular thalamus. *Journal of Neuroscience*, 38(5):1232–1248, 2018.

[64] Carole E Landisman, Michael A Long, Michael Beierlein, Michael R Deans, David L Paul, and Barry W Connors. Electrical synapses in the thalamic reticular nucleus. *Journal of Neuroscience*, 22(3):1002–1009, 2002.

[65] Michael A Long, Carole E Landisman, and Barry W Connors. Small clusters of electrically coupled neurons generate synchronous rhythms in the thalamic reticular nucleus. *Journal of Neuroscience*, 24(2):341–349, 2004.

[66] Philip RL Parker, Scott J Cruikshank, and Barry W Connors. Stability of electrical coupling despite massive developmental changes of intrinsic neuronal physiology. *Journal of Neuroscience*, 29(31):9761–9770, 2009.

[67] Seung-Chan Lee, Saundra L Patrick, Kristen A Richardson, and Barry W Connors. Two functionally distinct networks of gap junction-coupled inhibitory neurons in the thalamic reticular nucleus. *Journal of Neuroscience*, 34(39):13170–13182, 2014.

[68] Timothy A Zolnik and Barry W Connors. Electrical synapses and the development of inhibitory circuits in the thalamus. *The Journal of physiology*, 594(10):2579–2592, 2016.

[69] Scott J Cruikshank, Hayato Urabe, Arto V Nurmikko, and Barry W Connors. Pathway-specific feedforward circuits between thalamus and neocortex revealed by selective optical stimulation of axons. *Neuron*, 65(2):230–245, 2010.

[70] Shane R Crandall, Scott J Cruikshank, and Barry W Connors. A corticothalamic switch: controlling the thalamus with dynamic synapses. *Neuron*, 86(3):768–782, 2015.

[71] Guoqiang Hou, Alison G Smith, and Zhong-Wei Zhang. Lack of intrinsic gabaergic connections in the thalamic reticular nucleus of the mouse. *Journal of Neuroscience*, 36(27):7246–7252, 2016.

[72] Yasunobu Murata and Matthew T Colonnese. Thalamic inhibitory circuits and network activity development. *Brain research*, 1706:13–23, 2019.

[73] Jordan O'Byrne and Karim Jerbi. How critical is brain criticality? *Trends in Neurosciences*, 45:820–837, 2022.

[74] Rosa I. Martinez-Garcia, Bettina Voelcker, Julia B. Zaltsman, Saundra L. Patrick, Tanya R. Stevens, Barry W. Connors, and Scott J. Cruikshank. Two dynamically distinct circuits driving inhibition in sensory thalamus. *Nature*, 583:813 – 818, 2020.

[75] Chaoming Wang, Shangyang Li, and Si Wu. Analysis of the neuron dynamics in thalamic reticular nucleus by a reduced model. *Frontiers in Computational Neuroscience*, 15, 2021.

[76] Lucius Cueni, Marco Canepari, Rafael Luján, Yann Emmenegger, Masahiko Watanabe, Chris T Bond, Paul Franken, John P Adelman, and Anita Lüthi. T-type ca2+ channels, sk2 channels and sercas gate sleep-related oscillations in thalamic dendrites. *Nature neuroscience*, 11(6):683–692, 2008.

[77] Gil Vantomme, Alejandro Osorio-Forero, Anita Lüthi, and Laura MJ Fernandez. Regulation of local sleep by the thalamic reticular nucleus. *Frontiers in neuroscience*, 13:576, 2019.

[78] Laura MJ Fernandez, Gil Vantomme, Alejandro Osorio-Forero, Romain Cardis, Elidie Béard, and Anita Lüthi. Thalamic reticular control of local sleep in mouse sensory cortex. *Elife*, 7:e39111, 2018.

[79] DIEGO Contreras, R Curro Dossi, and MIRCEA Steriade. Bursting and tonic discharges in two classes of reticular thalamic neurons. *Journal of neurophysiology*, 68(3):973–977, 1992.

[80] Sang-Hun Lee, G Govindaiah, and Charles L Cox. Heterogeneity of firing properties among rat thalamic reticular nucleus neurons. *The Journal of physiology*, 582(1):195–208, 2007.

[81] Yinqing Li, Violeta G Lopez-Huerta, Xian Adiconis, Kirsten Levandowski, Soonwook Choi, Sean K Simmons, Mario A Arias-Garcia, Baolin Guo, Annie Y Yao, Timothy R Blosser, et al. Distinct subnetworks of the thalamic reticular nucleus. *Nature*, 583(7818):819–824, 2020.

[82] Julie S. Haas, Baltazar Zavala, and Carole E Landisman. Activity-dependent long-term depression of electrical synapses. *Science*, 334:389 – 393, 2011.

[83] David A McCormick. Cholinergic and noradrenergic modulation of thalamocortical processing. *Trends in neurosciences*, 12(6):215–221, 1989.

[84] David A McCormick. Neurotransmitter actions in the thalamus and cerebral cortex and their role in neuromodulation of thalamocortical activity. *Progress in neurobiology*, 39(4):337–388, 1992.

[85] Vincenzo Crunelli, Magor L Lőrincz, William M. Connelly, François David, Stuart W. Hughes, Régis C. Lambert, Nathalie Leresche, and Adam C. Errington. Dual function of thalamic low-vigilance state oscillations: rhythm-regulation and plasticity. *Nature Reviews Neuroscience*, 19:107–118, 2018.

[86] Giri Panamoottil Krishnan, Sylvain Chauvette, Isaac Shamie, Sara Soltani, Igor Timofeev, Sydney S. Cash, Eric Halgren, and Maxim Bazhenov. Cellular and neurochemical basis of sleep stages in the thalamocortical network. *eLife*, 5, 2016.

[87] Florin Amzica, A. Nún~ez, and Mircea Steriade. Delta frequency (1–4 hz) oscillations of perigeniculate thalamic neurons and their modulation by light. *Neuroscience*, 51:285–294, 1992.

[88] Simone Astori, Ralf D Wimmer, Haydn M Prosser, Corrado Corti, Mauro Corsi, Nicolas Liaudet, Andrea Volterra, Paul Franken, John P Adelman, and Anita Lüthi. The cav3. 3 calcium channel is the major sleep spindle pacemaker in thalamus. *Proceedings of the National Academy of Sciences*, 108(33):13823–13828, 2011.

[89] Chiara Pellegrini, Sandro Lecci, Anita Lüthi, and Simone Astori. Suppression of sleep spindle rhythmogenesis in mice with deletion of cav3. 2 and cav3. 3 t-type ca2+ channels. *Sleep*, 39(4):875–885, 2016.

[90] Stuart M. Fogel and Carlyle T. Smith. The function of the sleep spindle: A physiological index of intelligence and a mechanism for sleep-dependent memory consolidation. *Neuroscience & Biobehavioral Reviews*, 35:1154–1165, 2011.

[91] Róbert Bódizs, Tamás Kis, Alpar S. Lázár, L Havran, Péter Rigó, Zsófia Clemens, and Péter Halász. Prediction of general mental ability based on neural oscillation measures of sleep. *Journal of Sleep Research*, 14, 2005.

[92] Julie Seibt, Igor Timofeev, Julie Carrier, and Adrien Peyrache. Role of spindle oscillations across lifespan in health and disease. *Neural Plasticity*, 2016, 2016.

[93] Dagmara Panas, Urszula Malinowska, Tadeusz Piotrowski, Jarosław Żygierewicz, and Piotr Suffczyński. Statistical analysis of sleep spindle occurrences. *PLoS One*, 8(4):e59318, 2013.

[94] Giri P Krishnan, Burke Q Rosen, Jen-Yung Chen, Lyle Muller, Terrence J Sejnowski, Sydney S Cash, Eric Halgren, and Maxim Bazhenov. Thalamocortical and intracortical laminar connectivity determines sleep spindle properties. *PLoS computational biology*, 14(6):e1006171, 2018.

[95] Adrien Peyrache. In humans, sleep spindles are generated by local thalamic pacemakers. *The Journal of physiology*, 598(11):2041–2042, 2020.

[96] Denise Kohmann, Annika Lüttjohann, T. Seidenbecher, Philippe Coulon, and Hans-Christian Pape. Short-term depression of gap junctional coupling in reticular thalamic neurons of absence epileptic rats. *The Journal of Physiology*, 594, 2016.

[97] Philippe Coulon and Carole E Landisman. The potential role of gap junctional plasticity in the regulation of state. *Neuron*, 93:1275–1295, 2017.

[98] Chung-Kang Peng, Shlomo Havlin, Harry Eugene Stanley, and Ary L. Goldberger. Quantification of scaling exponents and crossover phenomena in nonstationary heartbeat time series. *Chaos*, 5 1:82–7, 1995.

[99] Mojtaba Bandarabadi, Carolina Gutierrez Herrera, Thomas C. Gent, Claudio L. A. Bassetti, Kaspar Anton Schindler, and Antoine R. Adamantidis. A role for spindles in the onset of rapid eye movement sleep. *Nature Communications*, 11, 2020.

[100] Pablo Fuentealba, Sylvain Crochet, Igor Timofeev, Maxim Bazhenov, Terrence J Sejnowski, and Mircea Steriade. Experimental evidence and modeling studies support a synchronizing role for electrical coupling in the cat thalamic reticular neurons in vivo. *European Journal of Neuroscience*, 20(1):111–119, 2004.

[101] Carole E Landisman and Barry W. Connors. Long-term modulation of electrical synapses in the mammalian thalamus. *Science*, 310:1809 – 1813, 2005.

[102] Ralf D. Wimmer, Lukas Ian Schmitt, Thomas J. Davidson, Miho Nakajima, Karl Deisseroth, and Michael M. Halassa. Thalamic control of sensory selection in divided attention. *Nature*, 526:705 – 709, 2015.

[103] Miho Nakajima, Lukas Ian Schmitt, and Michael M. Halassa. Prefrontal cortex regulates sensory filtering through a basal ganglia-to-thalamus pathway. *Neuron*, 103:445–458.e10, 2019.

[104] Zemin Wang, Ryan Neely, and Carole E Landisman. Activation of group i and group ii metabotropic glutamate receptors causes ltd and ltp of electrical synapses in the rat thalamic reticular nucleus. *The Journal of Neuroscience*, 35:7616 – 7625, 2015.

[105] Robert S. Morison and David L. Bassett. Electrical activity of the thalamus and basal ganglia in decorticate cats. *Journal of Nervous and Mental Disease*, 104:452, 1945.

[106] Igor Timofeev and Mircea Steriade. Low-frequency rhythms in the thalamus of intact-cortex and decorticated cats. *Journal of neurophysiology*, 76 6:4152–68, 1996.

[107] Nima Dehghani, Sydney S. Cash, Chih Chuan Chen, Donald J. Hagler, Mingxiong Huang, Anders M. Dale, and Eric Halgren. Divergent cortical generators of meg and eeg during human sleep spindles suggested by distributed source modeling. *PLoS ONE*, 5, 2010.

[108] Maxime Bonjean, Tanya I. Baker, Maxim Bazhenov, Sydney S. Cash, Eric Halgren, and Terrence J. Sejnowski. Interactions between core and matrix thalamocortical projections in human sleep spindle synchronization. *The Journal of Neuroscience*, 32:5250 – 5263, 2012.

[109] Giovanni Piantoni, Eric Halgren, and Sydney S. Cash. The contribution of thalamocortical core and matrix pathways to sleep spindles. *Neural Plasticity*, 2016, 2016.

[110] Amr Ayoub, Dominic Aumann, Anne Hörschelmann, Atossa Kouchekmanesch, Pia Paul, Jan Born, and Lisa Marshall. Differential effects on fast and slow spindle activity, and the sleep slow oscillation in humans with carbamazepine and flunarizine to antagonize voltage-dependent na+ and ca2+ channel activity. *Sleep*, 36 6:905–11, 2013.

[111] Miho Nakajima, L Ian Schmitt, and Michael M Halassa. Prefrontal cortex regulates sensory filtering through a basal ganglia-to-thalamus pathway. *Neuron*, 103(3):445–458, 2019.

[112] Maxim Bazhenov, Igor Timofeev, Mircea Steriade, and Terrence J Sejnowski. Model of thalamocortical slow-wave sleep oscillations and transitions to activated states. *Journal of neuroscience*, 22(19):8691–8704, 2002.

[113] Maxim Bazhenov, Igor Timofeev, Mircea Steriade, and Terrence J Sejnowski. Cellular and network models for intrathalamic augmenting responses during 10-hz stimulation. *Journal of Neurophysiology*, 79(5):2730–2748, 1998.

[114] Chaoming Wang, Tianqiu Zhang, Xiaoyu Chen, Sichao He, Shangyang Li, and Si Wu. Brainpy, a flexible, integrative, efficient, and extensible framework for general-purpose brain dynamics programming. *eLife*, 12:e86365, dec 2023.

[115] Chaoming Wang, Tianqiu Zhang, Sichao He, Yifeng Gong, Hongyaoxing Gu, Shangyang Li, and Si Wu. A differentiable brain simulator bridging brain simulation and brain-inspired computing. *arXiv preprint arXiv:2311.05106*, 2023.

[116] Alexandre Gramfort, Martin Luessi, Eric Larson, Denis A. Engemann, Daniel Strohmeier, Christian Brodbeck, Roman Goj, Mainak Jas, Teon Brooks, Lauri Parkkonen, and Matti S. Hämäläinen. MEG and EEG data analysis with MNE-Python. *Frontiers in Neuroscience*, 7(267):1–13, 2013.

[117] Karine Lacourse, Jacques Delfrate, Julien Beaudry, Paul Peppard, and Simon C Warby. A sleep spindle detection algorithm that emulates human expert spindle scoring. *Journal of neuroscience methods*, 316:3–11, 2019.

[118] Raphael Vallat and Matthew P Walker. An open-source, high-performance tool for automated sleep staging. *Elife*, 10:e70092, 2021.

[119] John M. Beggs and Dietmar Plenz. Neuronal avalanches in neocortical circuits. *The Journal of Neuroscience*, 23:11167 – 11177, 2003.

[120] Shan Yu, Andreas Klaus, Hongdian Yang, and Dietmar Plenz. Scale-invariant neuronal avalanche dynamics and the cut-off in size distributions. *PLoS ONE*, 9, 2014.

[121] Jeff Alstott, Edward T. Bullmore, and Dietmar Plenz. powerlaw: A python package for analysis of heavy-tailed distributions. *PLoS ONE*, 9, 2013.

[122] Aaron Clauset, Cosma Rohilla Shalizi, and Mark E. J. Newman. Power-law distributions in empirical data. *SIAM Rev.*, 51:661–703, 2007.

[123] M Steriade, L Domich, and G Oakson. Reticularis thalami neurons revisited: activity changes during shifts in states of vigilance. *Journal of Neuroscience*, 6(1):68–81, 1986.

[124] JR Huguenard and DA Prince. A novel t-type current underlies prolonged ca (2+)-dependent burst firing in gabaergic neurons of rat thalamic reticular nucleus. *Journal of Neuroscience*, 12(10):3804–3817, 1992.

[125] Thierry Bal and DAVID A McCORMICK. Mechanisms of oscillatory activity in guinea-pig nucleus reticularis thalami in vitro: a mammalian pacemaker. *The Journal of Physiology*, 468(1):669–691, 1993.

[126] Rodolfo R Llinás and Mircea Steriade. Bursting of thalamic neurons and states of vigilance. *Journal of neurophysiology*, 95(6):3297–3308, 2006.

[127] Mircea Steriade, David A McCormick, and Terrence J Sejnowski. Thalamocortical oscillations in the sleeping and aroused brain. *Science*, 262(5134):679–685, 1993.

[128] Laura D Lewis, Jakob Voigts, Francisco J Flores, L Ian Schmitt, Matthew A Wilson, Michael M Halassa, and Emery N Brown. Thalamic reticular nucleus induces fast and local modulation of arousal state. *elife*, 4:e08760, 2015.

[129] Pablo Fuentealba, Igor Timofeev, and Mircea Steriade. Prolonged hyperpolarizing potentials precede spindle oscillations in the thalamic reticular nucleus. *Proceedings of the National Academy of Sciences of the United States of America*, 101 26:9816–21, 2004.